Bull. Mater. Sci. (2023) 46:196
https://doi.org/10.1007/s12034-023-03031-0

Ca-induced changes in the crystal structure and magnetic properties of barium hexaferrite

S VERMA[1], A SINGH[1], S K GODARA[2], J AHMED[3], SM ALSHEHRI[3] and M SINGH[1,*]

[1]Department of Physics, Guru Nanak Dev University, Amritsar 143005, India
[2]Department of Chemistry, Guru Nanak Dev University, Amritsar 143005, India
[3]Department of Chemistry, College of Science, King Saud University, 11451 Riyadh, Saudi Arabia
*Author for correspondence (jmskhalsa@gmail.com)

MS received 31 January 2023; accepted 22 May 2023

Abstract. Ca-doped barium hexaferrite ($Ba_{1-x}Ca_xFe_{12}O_{19;}$ x = 0.1–0.6) samples were synthesized successfully using solid-state reaction route. Further, the limit of the Ca solubility in $BaFe_{12}O_{19}$ has been investigated in the 900–1200°C temperature range. X-ray analysis reveals maximum Ca solubility in BFO at 1200°C (≈50%). The emergence of a hematite secondary phase at Ca concentrations ≈50 and 60 at% was observed. The XRD analysis also confirmed a gradual reduction in the c-parameter from 23.195 Å (at x = 0.1) to 23.147 Å (at x = 0.5). The structural data further suggested an enhancement of sample density with Ca substitution. Field-emission transmission electron microscopy micrographs reveal (a) distinct grain morphology at lower Ca concentration (x = 0.1) and (b) enhanced secondary grain growth and grain amalgamation at higher Ca concentration (x = 0.5). The M–H studies reveal that M_r and M_s almost stay constant up to x = 0.2, beyond which they start rising rapidly. $M_r \approx 42.65$ emu g^{-1} and $M_s \approx 92.19$ emu g^{-1}, exhibit a maximum at x = 0.4. The coercivity first decreases rapidly from 4168 Oe (at x = 0.0) to 2326 Oe (at x = 0.1) followed by a marginal decrease to 2045 Oe (at x = 0.4). An H_c value ≥1200 Oe in a majority of our samples makes them potentially suitable for perpendicular recording media and permanent magnet applications.

Keywords. M-type barium hexaferrites; solid-state reaction route; X-ray diffraction; rietveld analysis; surface and elemental morphology; magnetic properties.

1. Introduction

Ferrites have emerged as very effective electrical and magnetic materials due to their appealing physical characteristics and for being applicable in manifold fields of ferrofluids, magnetic recording media, catalysis, diagnostic imaging and biomedical fields, and electrical devices, especially in microwave/GHz frequencies [1]. The characteristics that make hexagonal technologically promising candidates are (a) low dielectric constant, (b) high resistivity, (c) high saturation magnetization, (d) high coercivity and (e) their chemically stable nature [2]. The excellence of their electric and magnetic characteristics owes to the stacking variation of various metallic ions present in their crystal structure [3]. The properties of hexaferrites can hence be manipulated by partially substituting these cations using foreign dopants. Among M, X, U, W, Z and Y hexaferrites, M-type hexaferrites (with $MFe_{12}O_{19}$ as general formula, M denotes any metal of the second group of the periodic table) are widely chosen since they are easier to synthesize [4]. For this class of hexaferrites, resistivity and coercivity are superior, magneto anisotropy is quite high, and electrical conductivity is low [5]. They are highly chemical stable and most importantly, they are affordable and thus commercially viable [6,7]. As a consequence, they are among the best contenders to be utilized in domestic appliances also. They are majorly applicable in the areas of loudspeakers, shielding devices, capacitors, refrigerator door magnet, magnetic resonance imaging, memory cells, radar systems, transformers, multichip inductors, etc. [8–12]. As far as the production of the materials for permanent magnets is concerned, an estimated 90% (out of the total) weight is accounted for M-type hexaferrites [13].

A single BFO unit cell consists of 38 oxygen ions (O^{2-}), 2 barium ions (Ba^{2+}), 24 iron ions (Fe^{3+}) in total [5]. Their magnetic properties stem from Fe^{3+} ions which occupy trigonal bipyramidal, tetrahedral and octahedral sites (typically named 2b; 4f1; 12k, 2a and 4f2) [14–16]. These five spin sites are further grouped into two categories (a) spin-up (2a, 2b, 12k) and (b) spin-down (4f1 and 4f2) sites [17]. The distribution of Fe^{3+} ions into spin-up and spin-down sites results in a reduction of magnetic moment because of the cancellation of spin moments [18–20]. The magnetic characteristics of BFO can be modified by altering relative concentration of Fe^{3+} cations in these spin-up and spin-down sites [17,21–32]. However, A-site doping has also been

Published online: 27 September 2023

increasingly employed to modify various hexaferrite characteristics. Ca (either by itself and also in combination) has also been used to modify the magnetic properties of a number of M-type ferrites [22,23,31,32]. Popa *et al* [33] studied grain size variation in 5 to 20 min thermal-treated (between 800 and 1000°C) pure and 1 mol Ca-doped BFO and SrFO systems and their magnetic properties. An enhancement of coercivity in the SrFO system was reported [33]. Ali *et al* [34] used sol–gel autocombustion method to synthesize $Ba_{1-x}Ca_xFe_{11.5}Cr_{0.5}O_{19}$ (x = 0.0–0.5) samples and investigated their structural, microstructural and magnetic characteristics. Hematite impurity was observed in all the samples. The highest value of $H_c \approx 4306$ Oe was reported at $x = 0.5$ [34]. Khan *et al* [2] prepared $Ba_{0.5-x}Ca_{0.5}Pr_xNi_yFe_{12-y}O_{19}$ (x = 0.00–0.10 and y = 0.00–1.00) using sol–gel autocombustion technique. $M_s \approx 37.08$ emu g^{-1} and $H_c \approx 1645$ Oe were reported for $x = 0.5$ [2]. Ashima *et al* [35,36] reported the characterization of $Ba_{1-x}Ca_xFe_{12}O_{19}$ (x = 0.0 and 0.5) synthesized using solid-state reaction method. Hematite was observed as an impurity phase for $x = 0.5$. The M_s decreased from 53.03 ($x = 0.0$) to 33.17 emu g^{-1} ($x = 0.5$) due to the effect of Ca doping into BFO. On the other hand, coercivity (H_c) increased with increasing Ca content from 2750 (x = 0.0) to 3200 Oe (x = 0.5). Kumar *et al* [18] investigated structural, elemental and magnetic properties for the $Ba_{1-x}Ca_xFe_{12}O_{19}$ for ($x = 0.00$–0.20) system synthesized using sol–gel method. The maximum value of M_s ($\approx$59.48 emu g^{-1}) has been observed for x = 0.05. Godara and group [8] synthesized $Ba_{1-x}Ca_xFe_{12}O_{19}$ (x = 0.00–0.50) samples using sol–gel autocombustion method. Samples calcined at 1200°C were claimed to be phase pure till x = 0.50. M_s was reported to increase from 63.85 (at $x = 0.00$) to 71.82 emu g^{-1} (at $x = 0.50$). A decreasing trend in the value of coercivity from $\approx$3765 Oe (for $x = 0.00$) to 1735 Oe (for $x = 0.50$) was reported [37].

In summary, some of these results in $Ba_{1-x}Ca_xFe_{12}O_{19}$ (Ca-substituted BFO) samples are in contrast to each other. For example, an increase in coercivity (with x) was observed by Ashima *et al* [35,36] to decrease in coercivity was observed by Godara and group [8]. The trend of their M_r and M_s values are also in contrast to each other. Further, the coercivity values reported by Ali *et al* [34] $\approx$4306 Oe at $x = 0.5$ to Khan *et al* [2] reported value of $\approx$1645 Oe (at $x = 0.5$). Therefore, it is worth studying the modification of magnetic properties of BFO upon Ca substitution in a wide composition range. We hereby present the modification of structural, microstructural and magnetic properties by substituting Ca in BFO ($Ba_{1-x}Ca_xFe_{12}O_{19}$) samples calcined at 1200°C for 6 h synthesized via solid-state reaction method.

2. Experimental

M-type barium hexaferrite $Ba_{1-x}Ca_xFe_{12}O_{19}$ (x = 0.1–0.6) powders were synthesized by means of a solid-state reaction route technique. The chemical reaction involved in the synthesis of $Ba_{1-x}Ca_xFe_{12}O_{19}$ sample is as follows:

$$(1-x)\ BaCO_3 + 6Fe_2O_3 + xCaCO_3 \rightarrow Ba_{1-x}Ca_xFe_{12}O_{19} + CO_2 \quad (1)$$

The starting materials ($BaCO_3$, $CaCO_3$ and Fe_2O_3) chosen for the synthesis of the required material were weighed according to their stoichiometric amount. Then these weighed materials were poured into a bottle suspended in an acetone medium having 20 zirconium balls. A 24-h period was spent combining these materials in a ball mill. The resulting blended powders were then allowed to air dry for around 12 h. Then a sintering procedure was conducted in a muffle furnace between 900 and 1200°C for 6 h. At last, the calcined powders were converted into fine powder using grinding using a mortar pestle.

The structural analysis of the prepared samples was examined by collecting their respective X-ray diffraction patterns/diffractograms. The X-ray patterns were collected using MAXIMA XRD-7000 from SHIMADZU within the scanned 2θ range (20°–80°; scan step size of 0.02°) having a scanning rate of 1° min^{-1}. FULLPROF SUITE software was employed to perform the Rietveld refinement. Field-emission transmission electron microscopy (FESEM) data was recorded (in pellet form) using Gemin SEM500 (from Carl Zeiss). The scale for the scanning images of these samples is 1 μm and the magnification is 25 Kx. The room temperature *M–H* data was recorded using EZ9 from Microsense.

3. Results and discussions

3.1 *Crystal structure determination*

As stated in the introductory text, the issue of Ca solubility in $BaFe_{12}O_{19}$ has been investigated in the 900–1200°C temperature range. In this regard, $Ba_{1-x}Ca_xFe_{12}O_{19}$ (x = 0.1–0.6) samples were synthesized using standard ceramic technique. However, the x = 0.5 sample was only calcined at 1100 and 1200°C. The issue of phase purity of these samples was addressed using Rietveld refinement of the XRD data. A nice match between the experimental and the refined data (low value of GoF, and random distribution of the difference data about mean) using a single-phase ($P6_3/mmc$ structural symmetry, (ICSD 98-010-5657)) model has been used as a criterion for affirming the phase purity of the sample under investigation. Any discrepancy between the experimental and refined data was seen as an indication of limitation of the single-phase/multiple-phase model, thereby implying the sample to be phase-impure.

The Rietveld refined (employing a single-phase structural model) data of 900°C calcined x = 0.2 and x = 0.6 samples are shown in figure 1a and c. The presence of unexplained peaks (only black data) in the main plot and sharp positive peaks in the difference plot is suggestive of the failure of the single-phase model to reasonably explain the diffraction data. It is to be noted that the above-stated discrepancies are

relatively much more pronounced in the $x = 0.6$ sample as compared to $x = 0.2$ sample. The single-phase χ^2-values ≈ 2.50 and 6.49 have been observed for $x = 0.2$ and 0.6, respectively. These discrepancies are indicative of the fact that the Ca solubility in $BaFe_{12}O_{19}$ is below 20 at% at 900°C. In order to further improve the refinement, multiple-phase Rietveld refinement was initiated. By comparing the mismatched peaks with the ICSD database, (a) Fe_2O_3 phase (ICSD 98-002-2616) was found to exist as an impurity in $x = 0.2$ and (b) Fe_2O_3 along with $Ca_2Fe_2O_5$ (ICSD 98-000-5960) phases were found to be present as impurity phases in $x = 0.4$ and 0.6 samples. The powder diffraction data for $x = 0.2$ was hence modeled by employing (Ca-doped BFO (*P6₃/mmc*) + Fe_2O_3 (*R-3c*)) phases and the refined data is shown in figure 1b. The two-phase model leads to an improvement in the χ^2-values from 2.50 to 1.50. Rietveld refined data using (Ca-doped BFO (*P6₃/mmc*) + Fe_2O_3 (*R-3c*) + $Ca_2Fe_2O_5$ (*Pnma*)) phases for $x = 0.6$ sample is shown in figure 1d. The multiple-phase fitting for this sample leads to a reduction in χ^2-values from 6.49 to 1.62. A similar approach was used to analyse the phase purity of $x = 0.2$–0.6 samples calcined at 900, 1000 and 1100°C. However, the Rietveld refined data has not been shown for all these samples. The parameters extracted from Rietveld refinement (phase fraction, space group and GoF) for all the samples (up to $x = 0.6$) calcined at ≤1100°C have been summarized in table 1. It is quite evident from table 1 that up to 40 at% Ca is soluble in BFO at 1100°C. Further in the $x = 0.6$ sample, the $Ca_2Fe_4O_5$ phase disappears at 1100°C and Fe_2O_3 phase (19.93%) persists. This implies that Ca solubility in BFO at 1100°C could be ≈40 at%.

The Rietveld refined data of Ca-doped BFO samples ($x = 0.1$–0.6) calcined at 1200°C is shown in figure 2a–f. However, the single-phase structural model was only found to be suitable up to $x = 0.4$. Beyond $x = 0.4$, Fe_2O_3 was observed as a phase impurity. Therefore, the structural data of the samples beyond $x = 0.4$ was refined using a two-phase (Ca-doped BFO and Fe_2O_3) model. The χ^2 (GoF) values

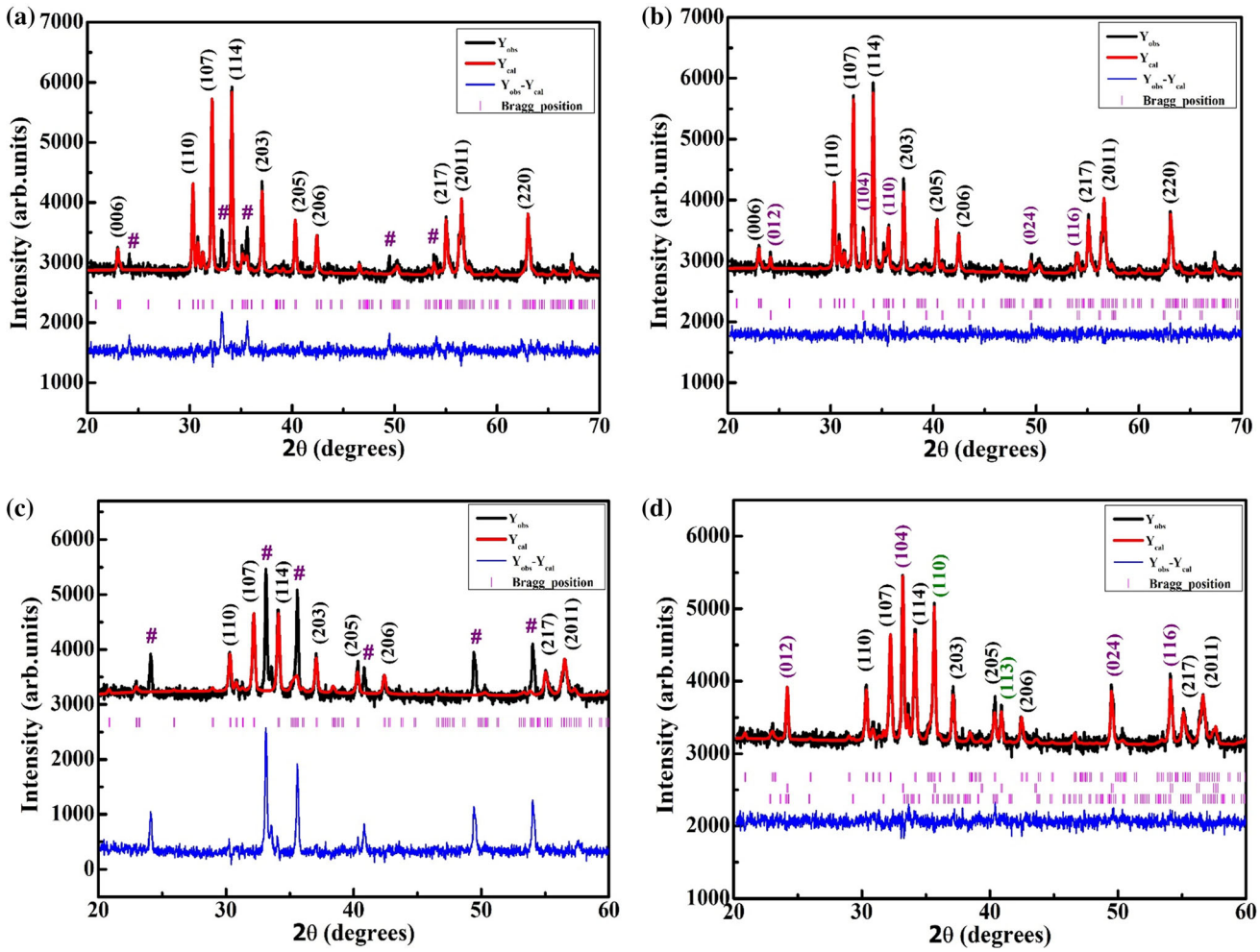

Figure 1. The Rietveld refined data of (**a**) $x = 0.2$ single phase, (**b**) $x = 0.2$ two-phase and (**c**) $x = 0.6$ single phase, (**d**) $x = 0.6$ three-phase $Ba_{1-x}Ca_xFe_{12-2x}O_{19}$ samples calcined at 900°C. The red/black curves represent experimental/Rietveld refined data. # represents the unidentified peaks. The (hkl) corresponding to the main phase has been marked in black colour and that of secondary phases Fe_2O_3 and $Ca_2Fe_2O_5$ in purple and green colour, respectively.

Table 1. Fractional percentage of various phases used along with their space groups and GoF obtained from Rietveld refinement in $x = 0.2$, 0.4, 0.5 and $0.6Ba_{1-x}Ca_xFe_{12}O_{19}$ samples calcined between 900 and 1100°C.

x	Calcination temperature (°C)	Phases	Space group	Fractional percentage	GoF
0.2	900	$BaFe_{12}O_{19}$	*P6₃/mmc*	89.13	1.50
		Fe_2O_3	*R-3c*	10.87	
	1000	$BaFe_{12}O_{19}$	*P6₃/mmc*	89.75	1.44
		Fe_2O_3	*R-3c*	10.25	
	1100	$BaFe_{12}O_{19}$	*P6₃/mmc*	100	1.48
0.4	900	$BaFe_{12}O_{19}$	*P6₃/mmc*	71.65	1.47
		Fe_2O_3	*P6₃/mmc*	25.73	
		$Ca_2Fe_2O_5$	*Pnma*	2.62	
	1000	$BaFe_{12}O_{19}$	*P6₃/mmc*	82.71	1.48
		Fe_2O_3	*R-3c*	14.55	
		$Ca_2Fe_2O_5$	*Pnma*	2.74	
	1100	$BaFe_{12}O_{19}$	*P6₃/mmc*	100	1.62
0.5	1100	$BaFe_{12}O_{19}$	*P6₃/mmc*	90.15	1.41
		Fe_2O_3	*R-3c*	9.85	
0.6	900	$BaFe_{12}O_{19}$	*P6₃/mmc*	56.68	1.62
		Fe_2O_3	*R-3c*	35.97	
		$Ca_2Fe_2O_5$	*Pnma*	7.35	
	1000	$BaFe_{12}O_{19}$	*P6₃/mmc*	57.79	1.65
		Fe_2O_3	*R-3c*	32.99	
		$Ca_2Fe_2O_5$	*Pnma*	9.22	
	1100	$BaFe_{12}O_{19}$	*P6₃/mmc*	77.99	1.62
		Fe_2O_3	*R-3c*	22.01	

$\approx$1.76, 1.43, 1.84, 1.45, 1.77 and 1.50 were obtained for $x = 0.1$, 0.2, 0.3, 0.4, 0.5 and 0.6 samples, respectively. This value of GoF is indicative of a good level of refinement [38]. Surprisingly, the fraction of Fe_2O_3 only increased from 5.90% (in $x = 0.5$ sample) to 6.57% (in $x = 0.6$ sample). This is because Ca-solubility $\approx$44 at% would have resulted in a segregation of around 16% Fe_2O_3 in the $x = 0.6$ sample. The observed discrepancy could either be due to chemical inhomogeneity or thermal fluctuations. In a nutshell, the XRD studies point to Ca solubility $\approx$50 a% in BFO.

The impact of Ca^{2+} substitution on the X-ray density (D_x), bulk density (D_b) and sample porosity (P) of these samples was also examined. Their values have been calculated using the formulae $D_x = \frac{ZM}{N_a V_{cell}}$, $D_b = \frac{m}{t\pi r^2}$ and $P = \left(\frac{D_x - D_b}{D_x}\right) \times 100$ [8]. The lattice parameters (a), (c), c/a ratio cell volume (V_{cell}), D_x, D_b and P of these samples are given in table 2. The incorporation of foreign ion/ions having different ionic radii into the BFO lattice might potentially affect the lattice parameters a and c. In this study, we observe (as given in table 2), lattice parameter (a) remains almost the same for all the compositions, whereas the lattice parameter (c) decreases marginally from 23.195 to 23.093 Å with an increase in the Ca concentration. This observed trend could be explained on the basis of the relative ionic radii of the host Ba^{2+} (1.34 Å) and doped Ca^{2+} (0.99 Å) ions. The substitution of a cation having lower ionic radii as compared to host ions will drive the remaining host ions closer to each other as the substituted ion occupies lesser space. As the host ions move close to each other, a net reduction in lattice parameters takes place. The lattice contraction may also be explained on the basis of empirical Vegard's law for any solid solutions A–B as [39].

$$a = a_A^0(1 - X) + a_B^0(X) \tag{2}$$

where $X = X_B$ is the mole fraction of component B and a_A^0 and a_B^0 are the lattice parameters of the pure components A and B, respectively. As per this law, if we are making solid solutions of two materials with one having higher ionic radii (and hence higher lattice parameters) and the other having lower ionic radii (and hence lower lattice parameters), the lattice parameters of the resulting solid solution will be average of the two extremes. The dopant-induced lattice expansion (where dopant atom has higher ionic radii) has been reported by a number of research groups [40–44]. In contrast, we are observed lattice contraction as we are substituting a dopant with lower ionic radii as compared to the host. This observed trend is better depicted in figure 3. The lattice parameter ratio (c/a) is a marker for determining the kind of hexaferrite. A ratio of less than 3.98 is an indicator of the M-type hexaferrite [45]. For our samples, the c/a ratio is less than 3.98 confirming that they are M-type hexaferrite. The X-ray density decreases from 5.24 to 5.05 g cm^{-3} with the increase in calcium concentration. Since, the X-ray density is directly

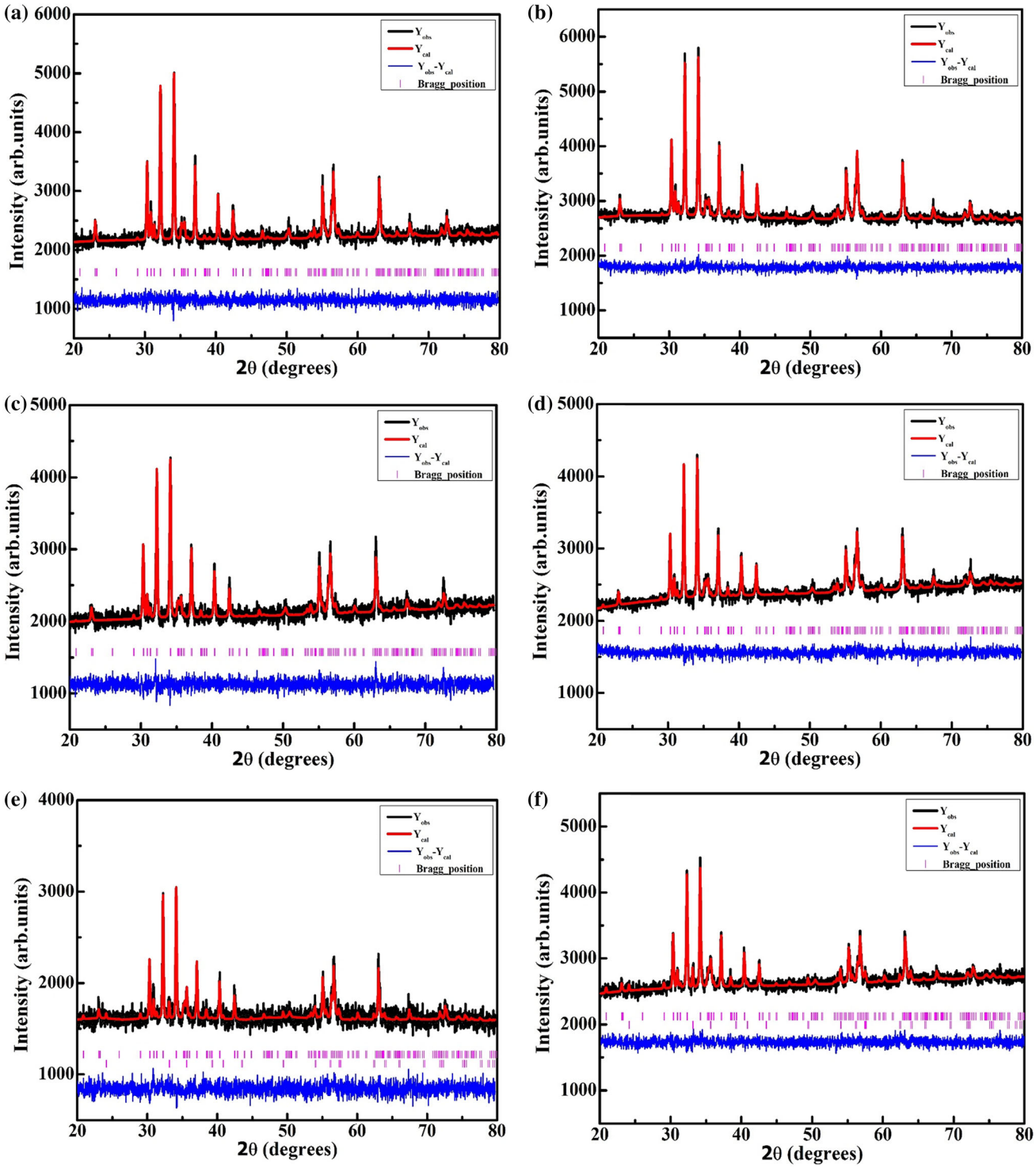

Figure 2. The Rietveld refined data of (**a**) $x = 0.1$, (**b**) $x = 0.2$, (**c**) $x = 0.3$, (**d**) $x = 0.4$, (**e**) $x = 0.5$ and (**f**) $x = 0.6$ $Ba_{1-x}Ca_xFe_{12-2x}O_{19}$ samples calcined at 1200°C. The red/black curves represent experimental/Rietveld refined data.

proportional to the atomic mass of the sample, the decrease in X-ray density could be due to the difference in the atomic masses of the doped calcium (Ca^{2+}) (40.078 amu) ion and host Ba^{2+} (137.33 amu) ion [34]. Conversely, bulk density increases with an increase in calcium concentration from 3.15 g cm^{-3} (at $x = 0.1$) to 3.69 (at $x = 0.5$) g cm^{-3}. This implies that enhanced Ca substitution results in a net reduction of the concentration of voids, which ultimately leads to enhanced bulk density [46]. The enhancement of sample densification is also apparent from the calculated porosity (P) values, which decrease from 37% at $x = 0.1$ to 23% at $x = 0.5$. Thus, in summary, XRD measurements

Table 2. Structural parameters, *c/a* ratio, X-ray density (D_x), bulk density (D_b) and porosity (P) of $Ba_{1-x}Ca_xFe_{12}O_{19}$ samples. S.P. and D.P. denote single- and double-phase structural models, respectively.

x		a (Å)	c (Å)	c/a	V_{cell} (Å^3)	D_x (g cm^{-3})	D_b (g cm^{-3})	P (%)	GoF
0.1		5.895	23.195	3.93	697.999	5.24	3.15	37	1.76
0.2		5.891	23.170	3.93	696.581	5.05	3.20	36	1.43
0.3		5.893	23.161	3.93	696.785	5.00	3.41	32	1.84
0.4		5.894	23.154	3.93	696.778	4.93	3.52	29	1.45
0.5	BFO	5.895	23.147	3.92	696.553	5.07	3.95	24	1.83(S.P.)
	Fe_2O_3	5.039	13.773	2.73	302.980	5.25			1.77(D.P.)
0.6	BFO	5.885	23.093	3.92	696.287	5.05	3.69	23	1.92(S.P.)
	Fe_2O_3	5.040	13.773	2.72	303.674	5.25			1.50(D.P.)

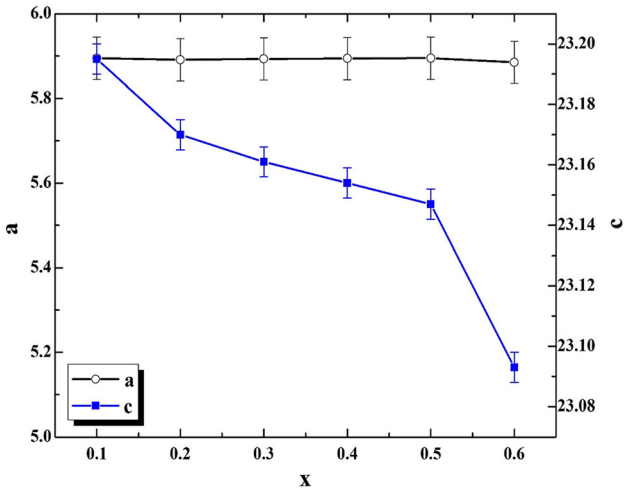

Figure 3. Variation of lattice parameters (**a** and **c**) with composition in $Ba_{1-x}Ca_xFe_{12-2x}O_{19}$ samples calcined at 1200°C.

confirm (a) Ca solubility in BFO is ≈50%, (b) the emergence of secondary phases at Ca concentrations ≈50 and 60 at%, (c) gradual reduction in the value of *c*-parameter and (d) the enhancement of sample density.

In the literature reports, only Ashima *et al* [35] reported Fe_2O_3 as a secondary phase impurity in the 50 at% Ca-substituted BFO samples. Most of the other authors [2,18,47] reported phase purity up to 50 at% Ca substitution in BFO. The differences could be due to the use of different synthesis techniques, calcination temperature and duration. Also, similar to Godara and group [8] we observe lattice contraction with increasing Ca substitution [37].

3.2 *Microstructural studies*

The FESEM micrograph of the typical Ca-substituted barium hexaferrite samples (for x = 0.2, 0.4 and 0.5) is shown in figure 4a, b and c. It is clear from figure 4a that the x = 0.2 sample consists of grains with distinct grain boundaries. Further, (a) most of these grains appear to have plate-like shape and (b) some of them could be noticed to have boundaries varying from four to six. A very little amount of secondary growth could also be noticed by the presence of very small-sized round-shaped grains. The average grain size in this sample is ≈0.21 μm. The secondary grain growth appears to be more dominant in the x = 0.4 sample, as is evident from the presence of a large number of < 300 nm-sized grains. In this sample, the bigger (plate-like grains) with well-defined boundaries are also noticeable in the background. However, the secondary grains are obscuring most of the view. The average grain size (most of the smaller grains opt for the measurement as boundaries of larger grains are difficult to decipher) in this sample is ≈0.25 μm. In the x = 0.5 sample, no distinct grain boundaries between secondary grains and primary grains are visible. The image rather presents a fusion of smaller grains into larger grains. The fused kind of morphology observed in this sample could be a potential hint of maximum tolerable Ca concentration in BFO lattice between 40 and 50 at%. It is to be noticed that the presence of even a large number of secondary grains in x = 0.4 sample and the fusion of smaller and larger grains in the x = 0.5 sample make the estimation of average grain size rather difficult. The histogram giving the size distribution of the prepared samples is shown in figure 5a, b and c.

3.3 *Energy dispersive X-ray analysis*

Energy dispersive X-ray (EDX) spectrum of the typical $Ba_{1-x}Ca_xFe_{12}O_{19}$ hexaferrite sample (for x = 0.4) is shown in figure 6. The spectrum confirms the presence of barium, calcium, iron and oxygen in the prepared sample. The atomic percentages of various elements (also x = 0.2 and 0.5) have also been calculated from the EDX spectra and are given in table 3. The table also gives the values of the measured and expected Fe:Ba ratio. It is clear that the measured and expected Fe:Ba ratio exhibits a similar trend with increasing Ca concentration. The small differences between the experimental and expected Fe:Ba ratio could be due to the fact that the experiment values have been obtained using a standardless quantification approach.

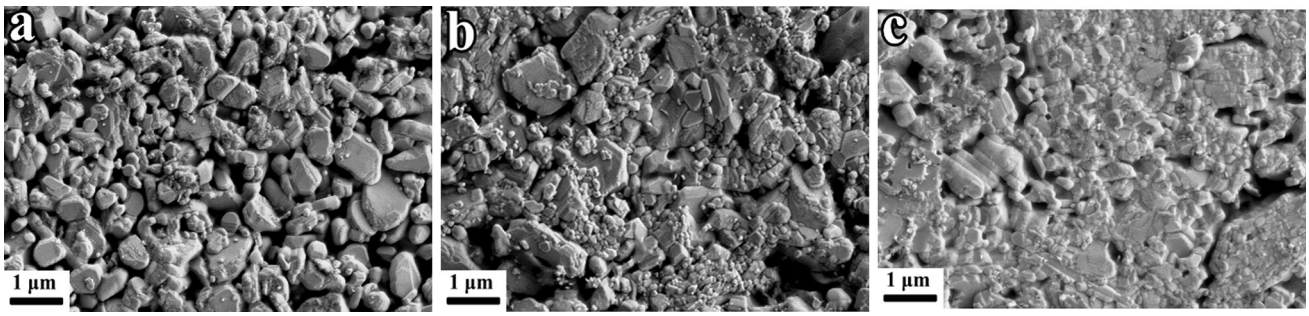

Figure 4. FESEM images of $Ba_{1-x}Ca_xFe_{12}O_{19}$ samples (**a**) x = 0.2, (**b**) x = 0.4 and (**c**) x = 0.5 calcined at 1200°C.

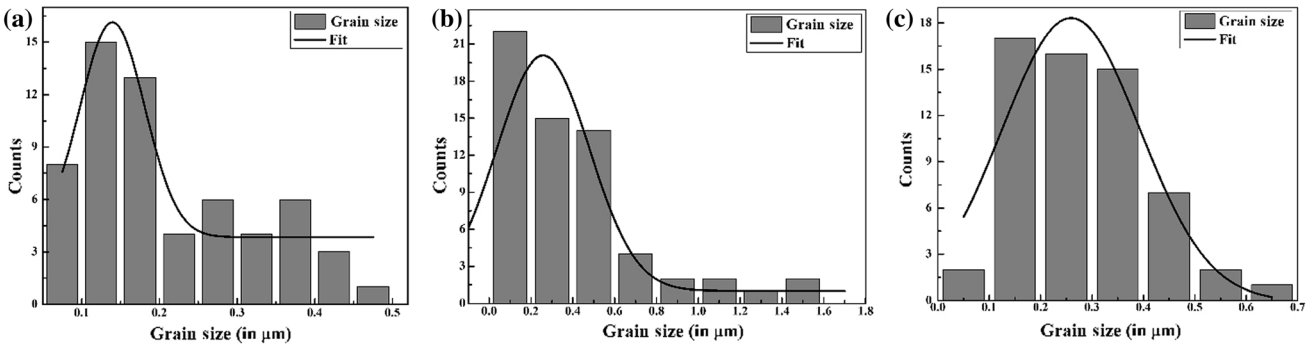

Figure 5. Histogram giving the size distribution of $Ba_{1-x}Ca_xFe_{12}O_{19}$ samples: (**a**) x = 0.2, (**b**) x = 0.4 and (**c**) x = 0.5 calcined at 1200°C.

3.4 *Magnetic studies*

Figure 7a, b depicts the room temperature M–H loops for x = 0.1–0.5 $Ba_{1-x}Ca_xFe_{12}O_{19}$ samples. The finite non-saturating loops unambiguously demonstrate that (a) all the samples possess hard ferrite characteristics and (b) have diminishing coercivity [48]. The remnant magnetization (M_r) and coercivity (H_c) of different samples were retrieved from the M–H loops (average of Y-axis intercept and X-axis intercept, respectively). The saturation magnetization (M_s) value was obtained by carrying out a plot between M *vs.* $1/H^2$ (law of approach to saturation method) [8,49]. The Y-axis intercept of the linear fit (shown in figure 8) to this data (between 12,000 to 15,000 Oe range) is taken as the M_s value. The magnetic parameters so extracted are given in table 4. The table clearly shows a monotonic increase in the value of M_s from 70.26 to 92.19 emu g^{-1},

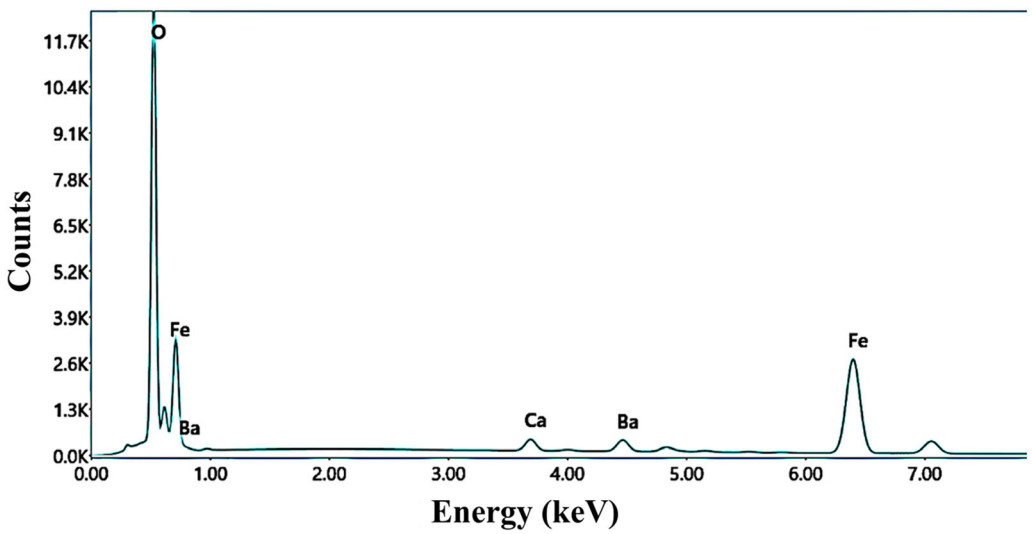

Figure 6. EDX spectra of x = 0.4 $Ba_{1-x}Ca_xFe_{12}O_{19}$ samples.

Table 3. Approximate atomic percentage of various elements in $Ba_{1-x}Ca_xFe_{12}O_{19}$ samples, calculated from the EDX.

	Atomic percent					
x	Ba	Ca	Fe	O	Fe/Ba (Meas.)	Fe/Ba (Exp.)
0.2	2.3	0.7	32.3	64.7	14.04	15
0.4	1.7	1.6	32.0	64.7	18.82	20
0.5	1.5	1.5	33.4	63.6	22.26	24

and a decrease in H_c from 2326 to 2045 Oe with an increase in the value of 'x'.

The M_r, M_s and H_c values for better elucidation are plotted as a function of increasing Ca-concentration (x) and are shown in figure 9a and b. It is clear from figure 9a that M_r and M_s almost stay constant up to $x = 0.2$, beyond which they start rising rapidly. The constant value of M_r and M_s up to $x = 0.2$ could be because Ca substitutes (a) mostly Ba-sites and (b) part of it substitutes equally between up-spin (2a, 2b and 12k) and down-spin (4f1 and 4f2) sites. As a consequence, the net distribution of 12 Fe^{3+} ions between up-spin and down-spin sites remains unaffected, thereby leading to an almost constant value of M_r and M_s. However, beyond $x = 0.2$, the Ca^{2+} ions in addition to occupying Ba sites also start preferably occupying down-spin Fe sites. As a consequence, there is a decrease in the value of magnetic moment contribution from down-spin Fe sites (which decrease the magnetic moment), which results in the enhancement of the value of M_r and M_s [50]. The small increase in the value of M_r and M_s at $x = 0.5$ could be due to the phase impurity present in this sample (as discussed in the XRD section) [35]. Also, the SEM data for this sample hinted at fused grain growth.

The coercivity value meanwhile decreases rapidly in the beginning from 4168 Oe ($x = 0.0$) to 2326 Oe ($x = 0.1$) and thereafter it decreases slightly to 2045 Oe ($x = 0.4$), as shown in figure 9b. The H_c variation can be somewhat explained in terms of varying values of k (magnetocrystalline anisotropy ($k = \frac{\mu_0 M_s H_c}{2}$); ($\mu_0$ (magnetic permeability of free space) is taken as unity in cgs units)) [51]. The k-values have also given in table 4 and plotted in figure 9b. It is clear from figure 9b that the decrease in H_c is in nearly direct correlation with a varying value of k. However, there is a slight difference between the minima in H_c (at $x = 0.4$) and the minima of k (at $x = 0.3$). The difference could be due to the type of atomic site being substituted by Ca. Microscopically, the initial rapid decrease in coercivity may be related to more preference for 4f2 and 2a (octahedral sites which have maximum contribution for magnetocrystalline anisotropy in hexaferrites) sites up to $x = 0.1$ [2,52,53]. As a result, M_r and M_s do not change but H_c decreases rapidly. Beyond $x = 0.1$, the other up-spin sites

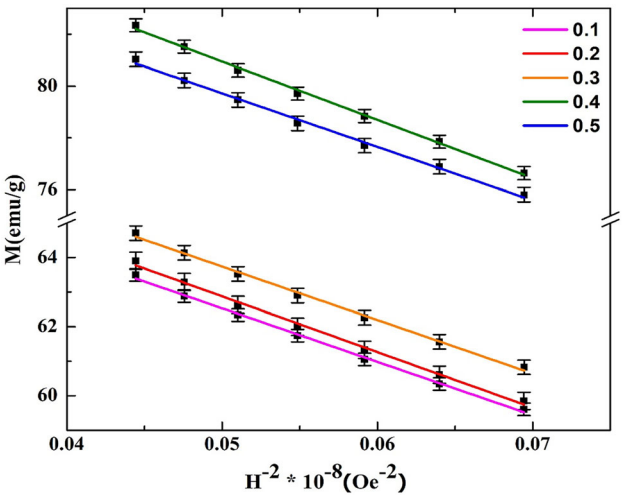

Figure 8. The M *vs.* $1/H^2$ plots along with the linear fitted data for $x = 0.1$–0.5 $Ba_{1-x}Ca_xFe_{12}O_{19}$ samples.

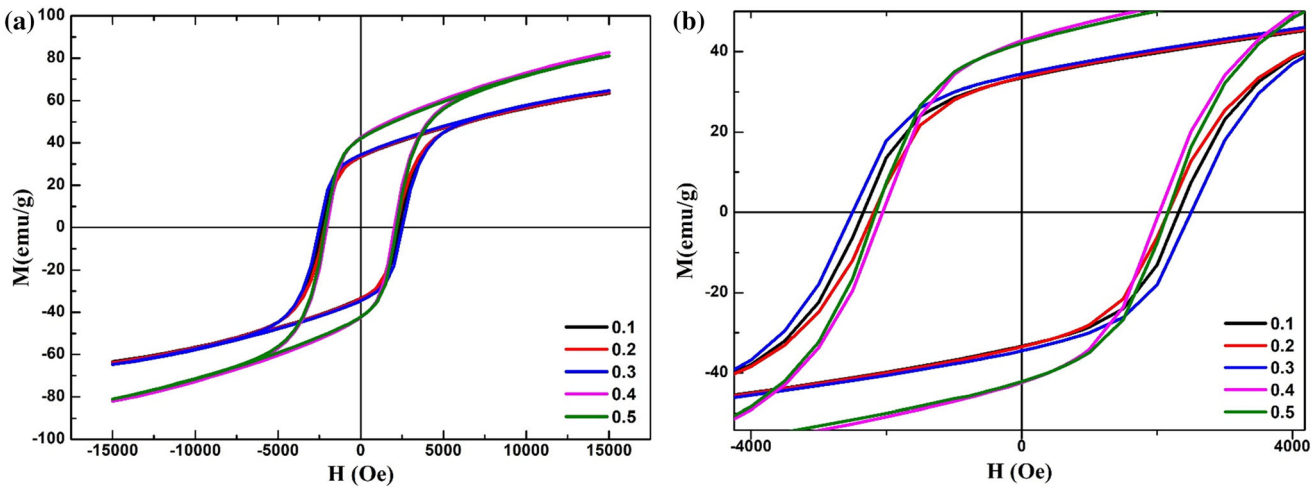

Figure 7. (**a**) The hysteresis (M–H) loops for $x = 0.1$–0.5 $Ba_{1-x}Ca_xFe_{12}O_{19}$ samples recorded at room temperature and (**b**) zoomed view of the hysteresis loops for $x = 0.1$–0.5 $Ba_{1-x}Ca_xFe_{12}O_{19}$ samples.

Table 4. M_r, H_c and M_s and k-values extracted for x = 0.1–0.5 $Ba_{1-x}Ca_xFe_{12}O_{19}$ samples.

x	H_c (± 0.2) (Oe)	M_r (± 0.12) (emu g^{-1})	M_s (± 0.21) (emu g^{-1})	M_r/M_s	k (Oe. emu g^{-1}) × 10^4
0 [8]	4168.02	33.55	69.85	0.48	14.38
0.1	2326.05	33.44	70.26	0.47	8.17
0.2	2173.65	33.54	70.93	0.47	7.71
0.3	2110.75	34.44	71.48	0.48	7.54
0.4	2045.25	42.65	92.19	0.46	9.42
0.5	2152.68	42.15	90.05	0.46	9.69

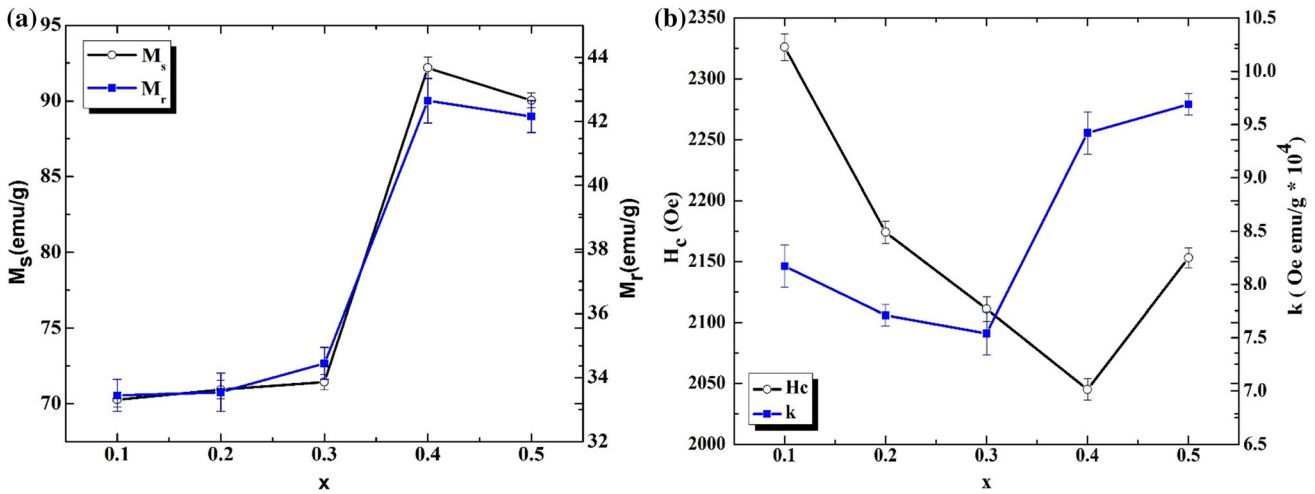

Figure 9. Variation of (**a**) M_s and M_r, and (**b**) H_c and k as a function of 'x'.

become slightly more preferred in addition to the 4f2 and 2a sites. As a result, M_r and M_s start to increase marginally, whereas H_c keeps decreasing slowly. At still higher values of x (up to x = 0.4), the spin-up sites become increasingly preferred in addition to 4f2 and 2a sites. As a result, M_r and M_s rise rapidly and H_c only decreases marginally. These results hence suggest that the preference of Ca ions for different Fe sites keeps on changing with increasing Ca concentration. The slight anomalous results of the x = 0.5 samples could be due to chemical inhomogeneity, thermal fluctuations and phase impurities [35]. It may be noted that samples with H_c value of ≈600 Oe are potentially used for longitudinal magnetic recording and those with $H_c \geq$ 1200 Oe are preferred for perpendicular recording media [2]. For this study, H_c is observed to be ≥1200 Oe in most of the samples. Hence, these samples may be better suited for perpendicular recording media and permanent magnets.

The squareness ratio (deduced by taking the ratio of M_r and M_s) tells about the single or multidomain nature of the ferrite material. If this ratio is lower than 0.5, the multidomain grains exist in the randomly oriented fashion in the prepared ferrite material [1,54,55]. In all our samples, this ratio is less than 0.5 implying they are multidomain.

Comparative detailed information of the magnetic parameters obtained by different researchers on Ca-substituted BFO samples (using different synthesis techniques and calcination parameters) is given in table 5. Among these reports, the highest H_c value (≈4752 Oe) has been reported by Huang *et al* [47] for x = 0.5 in samples synthesized using solid-state reaction method (like ours). In contrast, we observed almost 54% reduction in coercivity (≈2153 Oe) at this composition along with phase impurities. We actually observe a very narrow variation of coercivity from 2326 Oe (at x = 0.1) to 2045 Oe (at x = 0.4). The other researchers have reported an H_c value close to 2000 Oe (similar to ours) at this composition [37]. Godara and group [8] reported an H_c value (≈1729 Oe), which is lowered by 20% as compared to ours (≈2173 Oe). However, the M_s and M_r values reported by us are the highest among the compiled results.

4. Conclusions

M-type calcium-substituted barium hexaferrite samples were successfully synthesized via solid-state reaction technique. X-ray analysis reveals the presence of a single

Table 5. A comparison of magnetic parameters (H_c, M_r, M_s) along with synthesis details (technique, calcination temperature and duration) for x = 0, 0.2 and 0.5 $Ba_{1-x}Ca_xFe_{12}O_{19}$ samples reported by different research groups.

Author	Ca (at%)	M_s (emu g^{-1})	M_r (emu g^{-1})	H_c (Oe)	Synthesis technique	Calcination temperature/duration
Ashima *et al* [35,36]	0	53.04	25.47	2750	Solid-state reaction	1100°C/4 h
	50	33.17	16.66	2889		
Huang *et al* [47]	50	65.45	—	4752	Solid-state reaction	1250°C/3 h
Khan *et al* [2]	50	37.08	23.06	1645	Sol–gel autocombustion	1100°C/3 h
Kumar *et al* [18]	20	22.4	11.0	5720	Sol–gel autocombustion	1000°C/2 h
Yasmin *et al* [1]	50	—	—	—	Sol–gel autocombustion	1100°C/8 h
Godara and group [8]	20	66.95	32.94	2040	Sol–gel autocombustion	1200°C/6 h
	50	71.82	34.01	1729		
This study	20	70.93	33.54	2174	Solid-state reaction	1200°C/6 h
	50	90.05	42.15	2153		

M-type phase only up to x = 0.4 with Fe_2O_3 as phase impurity beyond x = 0.4. The χ^2-values ≈1.76, 1.43, 1.84, 1.45, 1.77 and 1.50 were obtained for x = 0.1, 0.2, 0.3, 0.4, 0.5 and 0.6 samples, respectively. The XRD data is indicative of ≈50 at% Ca solubility in BFO at 1200°C. A gradual reduction in the lattice parameter (c) from 23.195 Å (at x = 0.1) to 23.147 Å (at x = 0.5) is observed. This observed trend could be explained on the basis of the relative ionic radii of the host Ba^{2+} (1.34 Å) and doped Ca^{2+} (0.99 Å) ions. The structural data further suggested decreasing sample porosity from ≈37% at x = 0.1 to ≈23% at x = 0.5. FESEM micrographs show that at lower Ca concentrations (x = 0.1), the samples consist of discrete grains with insignificant secondary grain growth, while at higher Ca concentrations (x = 0.5), enhanced secondary grain growth and grain amalgamation are noticeable. The *M–H* investigations reveal nearly constant M_r and M_s up to x = 0.2, after which they start rising quickly. This might be because Ca largely substitutes for Ba-sites and that a portion of it substitutes equally for an up-spin (2a, 2b and 12k) and down-spin (4f1 and 4f2) sites. The coercivity value meanwhile decreases rapidly in the beginning from 4168 Oe (x = 0.0) to 2326 Oe (x = 0.1) and thereafter it decreases marginally to 2045 Oe (x = 0.4). This may be because up to x = 0.1, the octahedral sites (4f2 and 2a, which contribute most to the magnetocrystalline anisotropy in hexaferrites) may be preferred substitutional sites. Both M_r ≈42.65 emu g^{-1} and M_s ≈92.19 emu g^{-1} exhibit a maximum value at x = 0.4. The coercivity >1200 Oe observed in our samples could make these materials potentially suitable for perpendicular recording media and permanent magnet applications.

References

[1] Yasmin N, Zahid M, Khan H M, Hashim M, Islam M U, Yasmin S *et al* 2019 *J. Alloys Compd.* **774** 962

[2] Khan H M, Islam M U, Xu Y, Ashiq M N, Ali I, Iqbal M A *et al* 2014 *Ceram. Int.* **40** 6487

[3] Yuping L, Daxin B, Zhangzhong W, Zhang Y, Lizhao C, Guangcheng Z *et al* 2018 *J. Alloys Compd.* **734** 130

[4] Verma S, Chawla A, Pushkarna I, Singh A, Kumar S, Kumar D *et al* 2021 *Mater. Today Commun.* **27** 102291

[5] Pullar R C 2012 *Prog. Mater. Sci.* **57** 1191

[6] Mahmood S H, Dushaq G H, Bsoul I, Awawdeh M, Juwhari H K, Lahlouh B I *et al* 2014 *J. Appl. Math. Phys.* **02** 77

[7] Mosleh Z, Kameli P, Poorbaferani A, Ranjbar M and Salamati H 2016 *J. Magn. Magn. Mater.* **397** 101

[8] Verma S, Singh A, Sharma S, Kaur P, Godara S K, Malhi P S *et al* 2023 *J. Alloys Compd.* **930** 167410

[9] Singh V P, Jasrotia R, Kumar R, Raizada P, Thakur S, Batoo K M *et al* 2018 *World J. Condens. Matter Phys.* **08** 36

[10] Abbas W, Ahmad I, Kanwal M, Murtaza G, Ali I, Khan M A *et al* 2015 *J. Magn. Magn. Mater.* **374** 187

[11] Abdellahi M, Najfinezhad A, Samanadari S S, Khandan A and Ghayour H 2018 *Chin. J. Phys.* **56** 331

[12] Huang L, Huang R, Pang F, Li A, Huang G, Zhou X *et al* 2020 *RSC Adv.* **10** 18008

[13] Kumar S, Kumar R, Kaur N and Singh P 2021 *Results Phys.* **22** 103903

[14] Habanjar K, Shehabi H, Abdallah A M and Awad R 2020 *Appl. Phys. A Mater. Sci. Process.* **126** 1

[15] Singh H and Rajput J K 2020 *SN Appl. Sci.* **2** 1

[16] Iqbal M J, Ashiq M N and Gomez P H 2009 *J. Alloys Compd.* **478** 736

[17] Ounnunkad S 2006 *Solid State Commun.* **138** 472

[18] Kumar S, Supriya S, Pandey R, Pradhan L K, Singh R K and Kar M 2018 *J. Magn. Magn. Mater.* **458** 30

[19] Sláma J, Grusková A, Papánová M, Kevická D, Dosoudil R, Jančárik V *et al* 2004 *J. Magn. Magn. Mater.* **272–276** 385

[20] Trukhanov A V, Trukhanov S V, Panina L V, Kostishyn V G and Kazakevich I S 2017 *J. Magn. Magn. Mater.* **426** 487

[21] Tehrani M K, Ghasemi A, Moradi M and Alam R S 2011 *J. Alloys Compd.* **509** 8398

[22] Sözeri H, Küçük I and Özkan H 2011 *J. Magn. Magn. Mater.* **323** 1799

[23] Corral-Huacuz J C and Mendoza-Suárez G 2002 *J. Magn. Magn. Mater.* **242–245** 430

[24] Winotai P, Thongmee S and Tangab I M 2000 *Mater. Res. Bull.* **35** 1747
[25] Soman V V, Nanoti V M and Kulkarni D K 2013 *Ceram. Int.* **39** 5713
[26] Khademi F, Poorbafrani A, Kameli P and Salamati H 2012 *J. Supercond. Nov. Magn.* **25** 525
[27] Tokunaga Y, Kaneko Y, Okuyama D, Ishiwata S, Arima T, Wakimoto S *et al* 2010 *Phys. Rev. Lett.* **105** 17
[28] Leccabue F, Panizzieri R, Garcia S, Suarez N, Sanchez J L, Ares O *et al* 1990 *J. Mater. Sci.* **25** 2765
[29] Gregori M L, Pinho M S, Lima R C, Leandro J C S and Ogasawara T 2004 *Key Eng. Mater.* **264–268** 1229
[30] Belous A G, V'yunov O I, Pashkova E V, Ivanitskii V P and Gavrilenko O N 2006 *J. Phys. Chem. B* **110** 26477
[31] Kaur T, Kaur B, Bhat B H, Kumar S and Srivastava A K 2015 *Phys. B Condens. Matter* **456** 206
[32] Dhage V N, Mane M L, Keche A P, Birajdar C T and Jadhav K M 2011 *Phys. B Condens. Matter* **406** 789
[33] Popa P D, Rezlescu E, Doroftei C and Rezlescu N 2005 *J. Optoelectron. Adv. Mater.* **7** 1553
[34] Ali I, Islam M U, Awan M S, Ahmad M and Iqbal M A 2013 *J. Supercond. Nov. Magn.* **26** 3277
[35] Ashima, Sanghi S, Agarwal A and Reetu 2012 *J. Alloys Compd.* **513** 436
[36] Ashima Sanghi S, Agarwal A and Reetu, 2011 *AIP Conf Proc.* **1393** 137
[37] Kumar S, Singh M, Kaur V, Narang S B and Kumar A 2021 *Ceram. Int.* **47** 19271
[38] Toby B H 2006 *Powder Diffr.* **21** 67
[39] Jacob K T, Raj S and Rannesh L 2007 *Zeitschrift Fuer. Met. Res. Adv. Tech.* **98** 776
[40] Mamatha C, Krishnaiah M and Sreedhar B 2017 *Procedia Eng.* **215** 130
[41] Yadav R K and Chauhan P 2020 *Indian J. Pure Appl. Phys.* **57** 881
[42] Abasht B, Beitollahi A and Mirkazemi S M 2016 *J. Magn. Magn. Mater.* **420** 263
[43] Jin S, Yang Y, Medvedeva J E, Ireland J R, Metz A W, Ni J *et al* 2004 *J. Am. Chem. Soc.* **126** 13787
[44] Ji L, Jiang G, Wu D and Chen J 2020 *Mater. Res. Express* **7** 066103
[45] Wagner T R and Styranec T J 1998 *J. Solid State Chem.* **138** 313
[46] Maria K H, Choudhury S and Hakim M A 2013 *Int. Nano Lett.* **3** 1
[47] Huang K, Yu J, Zhang L, Xu J, Li P, Yang Z *et al* 2020 *J. Alloys Compd.* **825** 154072
[48] Chauhan C C, Kagdi A R, Jotania R B, Upadhyay A, Sandhu C S, Shirsath S E *et al* 2018 *Ceram. Int.* **44** 17812
[49] Brown W F 1940 *Phys. Rev.* **58** 736
[50] Yoon D H, Muksin and Raju K 2016 *J. Supercond. Nov. Magn.* **29** 439
[51] Lee J, Lee E J, Hwang T Y, Kim J and Choa Y H 2020 *Sci. Rep.* **10** 1
[52] Bhandari C, Flatté M E and Paudyal D 2021 *Phys. Rev. Mater.* **5** 9
[53] Jalili H, Aslibeiki B, Varzaneh A G and Chernenko V A 2019 *Beilstein J. Nanotechnol.* **10** 1348
[54] Katlakunta S, Meena S S, Srinath S, Bououdina M, Sandhya R and Praveena K 2015 *Mater. Res. Bull.* **63** 58
[55] Vinnik D A, Klygach D S, Zhivulin V E, Malkin A I, Vakhitov M G, Gudkova S A *et al* 2018 *J. Alloys Compd.* **755** 177